Ocean Dynamics
https://doi.org/10.1007/s10236-023-01538-y

Energetics during eddy shedding in the Gulf of Mexico

Haiyuan Yang[1,2] · Chen Yang[1,2] · Yongzheng Liu[1,2] · Zhaohui Chen[1,2]

Received: 3 May 2022 / Accepted: 3 January 2023

Abstract

Using the Estimating Circulation and Climate of the Ocean (ECCO) Phase II product, this study investigates the energetic characteristics during eddy shedding in the Gulf of Mexico. Based on the sea level anomaly data between 1992 and 2016, a total of 34 eddy shedding events are identified. Drawing on multiscale energy and vorticity analysis method, the eddy kinetic energy (EKE) budgets are diagnosed based on the ensemble of 34 eddy shedding events. During the stage of eddy shedding, barotropic instability (BT) dominates the energy budget. Meanwhile, energy transfers from upper layer to the deep layer by vertical pressure work (PW), which is the main source of abyssal EKE. Before eddy detachment, cyclonic eddy appears at the southeastern side of the Loop Current. Even though buoyancy forcing (BF) dominates the energy budget, BT makes considerable contribution to the generation of cyclonic eddy. Baroclinic instability (BC) shares the similar horizontal distribution with BF which accounts for 32% of the value of BC.

Keywords Loop current · Eddy shedding · Barotropic instability · Energy budget · ECCO2

1 Introduction

The Gulf of Mexico (GM) is a marginal sea of the Atlantic Ocean. It is connected to the Caribbean Sea by the Yucatan Channel (YC) in the south and to the Atlantic Ocean by the Straits of Florida in the east (Fig. 1). The Loop Current (LC), which flows into the GM through YC with transport of 23 ~ 28 Sv (Candela et al. 2002; Sheinbaum et al. 2002; Athié et al. 2020), is the dominant feature of the circulation in the eastern GM (e.g., Oey et al. 2005). As part of the western boundary current of subtropical Atlantic, the LC has been proved to be important in regulating the variability of the oceanic circulation (Enfield et al. 2001; Xu et al. 2013; Buckley and Marshall 2016) and overlying atmosphere (e.g. Hong et al. 2000; Shay 2009).

Being an intense oceanic current, LC is characterized by large meander and pinched-off eddies. Based on both observations and model simulations, it is found that the LC experiences an anticyclonic eddy (with diameters of 250 ~ 300 km) detachment every 3 ~ 18 months (Cooper et al. 1990; Forristall et al. 1992; Sturges and Leben 2000). Since the ideal numerical experiment by Hurlburt and Thompson (1980), researchers have explored the underlying dynamics of eddy shedding in the GM based on the accumulated observations and model data (e.g., Vukovich 1988; Sturges 1994; Oey 1996; Sturges and Leben 2000; Vukovich 2007; Chang and Oey 2011, 2012; Liu et al. 2016; Lugo-Fernández et al. 2016; Weisberg and Liu 2017; Chiri et al. 2019). By now, several mechanisms have been proposed and can be divided into the following three categories. The first group (Pichevin-Nof mechanism; Pichevin and Nof 1997; Nof 2005) attributes the eddy detachment to the competition between β effect and eddy growth rate. Fueled by the mass influx from the YC, the meander of the LC begins to develop. With the accumulation of water and negative potential vorticity, the meander keeps growing larger and thus forms an anticyclonic eddy. Finally, the eddy is pinched-off when the westward Rossby wave speed exceeding its growth rate. In this theory, LC transport through YC is the major factor that influences the eddy shedding. Rather than focusing on the meander, the second group treats the LC evolution and eddy shedding processes as the intrinsic oceanic variability of a nonlinear dynamical system. The characteristics of this system (shedding interval, eddy

Responsible Editor: Sheila Natalí Estrada

Haiyuan Yang and Chen Yang contributed equally to this paper.

✉ Yongzheng Liu
lyz@ouc.edu.cn

[1] Frontier Science Center for Deep Ocean Multispheres and Earth System (FDOMES) and Physical Oceanography Laboratory, Ocean University of China, Qingdao 266100, China

[2] Laoshan Laboratory, Qingdao 266237, China

Published online: 14 February 2023

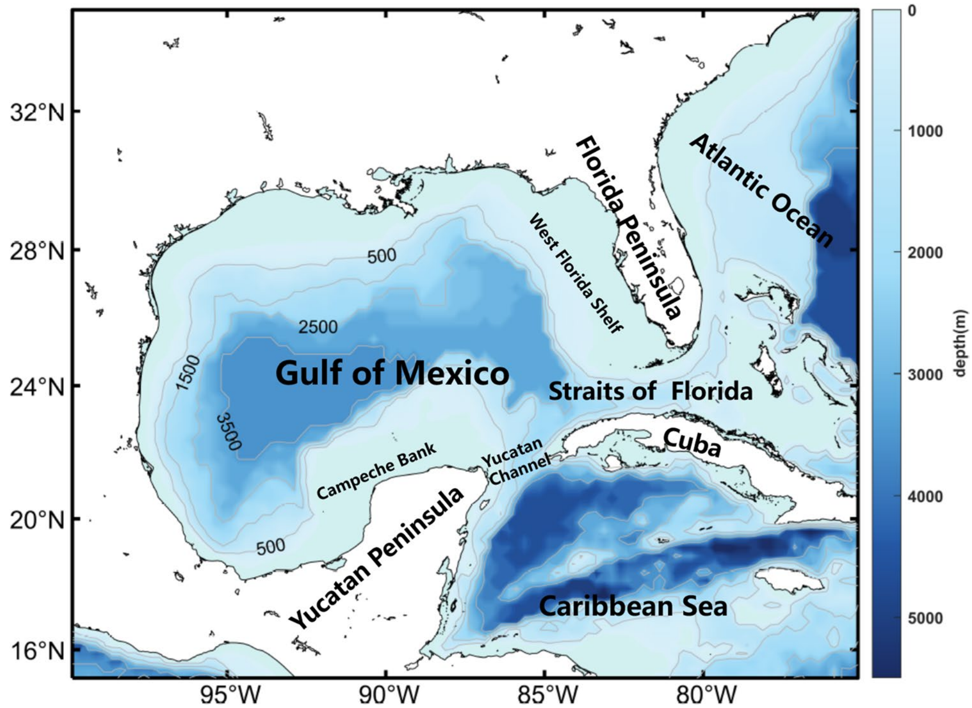

Fig. 1 Bathymetry (colored shading; unit: m) based on Estimating the Circulation and Climate of the Ocean, Phase II (ECCO2) in the Gulf of Mexico, Caribbean Sea, and western Atlantic Ocean. The isobaths of 500, 1500, 2500, and 3500 m are indicated by gray lines

size, and meander growth etc.) are regulated by several parameters (lateral viscosity, topography and inflow transport, etc.). On the basis of the above two theories, a lot of attention has been paid on the processes associated with YC transport, such as upstream flow (e.g., Welsh and Inoue 2000; Bunge et al. 2002; Chang and Oey 2011) and local wind field (e.g., Murphy et al. 1999; Candela et al. 2002; Oey 2004; Chang and Oey 2013). With the development of high-resolution observational methods and numerical models, the third group pays attention to the eddy-mean flow interaction in the GM, especially the energetics. Drawn energy from the inertial current, BC (e.g., Yin and Oey 2007; Oey 2008; Xu et al. 2013; Donohue et al. 2016; Hamilton 2019) and BT (Yang et al. 2020) are found to affect the meander growth and eddy formation based on the in situ data and model simulations. Yang et al. (2020) investigate the relative contributions of BT and BC during the formation of the eddy shedding. Yet, a work that addresses the evolution of energetics during the cycle of eddy shedding based on abundant eddy shedding events is still absent. On the one hand, suffering from the span coverage of mooring arrays, the observations in this region fail to provide a full picture of the eddy-mean flow energy transfer. On the other hand, energetic analyses based on high resolution models are mainly focused on long-term effect or state-mean value and thus cannot give insightful information about the energy exchange during the shedding processes. Therefore, it is necessary to revisit the energetics in this region, especially during the eddy shedding processes.

In addition to the 100-km-scale anti-cyclonic eddy, observations also capture cyclonic eddies in the vicinity of the LC meander (e.g., Cochrane 1972; Paluszkiewicz et al. 1983; Hamilton 1992; Oey and Lee 2002). Cochrance (1972) is the first scholar to find two cyclonic eddies locating at the west of the LC near the Campeche Bank and the east of the LC near the West Florida Shelf, respectively. Subsequent studies further indicate that these cyclonic eddies are generated at any time of the LC cycle with an irregular period of 75 days (Hurlburt 1986), which contributes to the detachment of eddy from LC (Cochrane 1972; Vukovich and Maul 1985; Fratantoni et al. 1998; Chérubin et al. 2006; Oey 2008; Le Hénaff et al. 2012; Huang 2013; Androulidakis et al. 2014; Rudnick et al. 2015). The generation of cyclonic eddy is investigated based on observation and model simulations. Oey (2008) shows that BC of the LC can generate the cyclonic eddy using a high-resolution numerical model. In an eddy-shedding case study based on observation and model, Xu et al. (2013) also find that small cyclones are caused by BC. On the other hand, Chérubin et al. (2006) suggest the contribution of BT in the generation of cyclonic eddy in the surface layers. By now, it remains unsolved that whether BT or BC dominates the generation of cyclonic eddy.

The abovementioned issues motivate us to investigate the energetics during the process of eddy shedding in the GM region. Here, we will focus on the energy exchange between mean flow and eddy during the shedding processes based on model product. The rest of paper is organized as follows: Sect. 2 and Sect. 3 briefly describe the data and analysis method, respectively. In Sect. 4, a detailed exploration of energetics associated with the eddy shedding in GM is presented. The discussion is in Sect. 5. This paper ends with a summary and conclusions in Sect. 6.

2 Data

2.1 Model data

In this study, Estimating the Circulation and Climate of the Ocean (ECCO) Phase II product (ECCO2, http://apdrc.soest.hawaii.edu/data/; cube92 version) is used. Based on the Massachusetts Institute of Technology General Circulation Model (MITgcm; Marshall et al. 1997), the global model solves the primitive equations on the cube-sphere grid with a horizontal resolution of 0.25° (Adcroft et al. 2004). It has 50 levels in vertical direction with thicknesses varying from 10 m near the surface to 456 m near the bottom. Quadratic drag law and biharmonic friction are used to parameterize the bottom stress and horizontal viscosity, respectively. The K-profile parameterization (KPP) vertical mixing scheme from Large et al. (1994) is employed to parameterize subgrid-scale vertical mixing processes. The eddy-permitting ECCO2 ocean state estimate is obtained by a least square fit of the MITgcm to available observations. Using the Green function approach (Menemenlis et al. 2005), the least squares fit is applied for number of model control parameters, initial conditions, and boundary conditions rather than modifying the data directly with artificial technics. With these optimized control parameters, the model is run forward freely without unphysical sources/sinks and artificial jumps. Thus, the solution is dynamically consistent and appropriate for process and budget analyses (Wunsch et al. 2009). The ECCO2 state estimate has been used to diagnose the eddy energetics both in the global ocean (Chen et al. 2014) and the Kuroshio Extension region (Yang et al. 2018). In this study, the 3-day-averaged dataset in the GM region (100°W–75°W, 15°N–35°N) from 1992 to 2016 is used.

2.2 Satellite observation

Satellite data can capture the characteristics of eddy shedding from LC (e.g., Zavala-Hidalgo et al. 2003; Athie et al. 2012). To validate the ECCO2 data in the GM region, the merged Sea Surface Height (SSH) product derived from measurements of several satellites (e.g., JASON-1 and 2, ENVISAT, ERS-1 and 2) is utilized in this study. This dataset is provided by Copernicus Marine Environment Monitoring Service (CMEMS, http://marine.copernicus.eu/) and is more efficient than the datasets using a single altimeter in resolving the mesoscale spatial and temporal variability of the ocean circulation (Ducet et al. 2000). The horizontal resolution of the absolute dynamic height (ADT) dataset is 0.25° at daily intervals. Similar to the ECCO2 data, the concurrent SSH fields during 1993–2016 within the region (100°W–75°W, 15°N–35°N) are analyzed in the study.

3 Method

In this study, eddy energetics of the eddy shedding in the GM region are analyzed using multiscale energy and vorticity analysis method (MS-EVA; Liang 2016). Based on wavelet analyses (Meyer wavelet is used in this study), MS-EVA decomposes time series into serval time-scale windows orthogonally without changing the total energy. Here, we decompose the variables into two windows where ~ 0 and ~ 1 represent mean flow and oceanic perturbations respectively:

$$A = A^{\sim 0} + A^{\sim 1} \tag{1}$$

The cutoff period should be divided by integer power of 2 according to the length of data (details refer to Liang 2016). The LC is found to shed eddy with an interval of 9 months, which will be discussed in Sect. 4.2. Therefore, the cutoff period which is calculated from the length and temporal resolution of the dataset is designed as 285 ($T/2 = 3044 \times 3/2^6 = 142.6875$) days for variables. Cyclonic eddies are generated at any time of the LC cycle with an irregular period of around 75 days (Hurlbut 1986). The cutoff period is designed as 72 ($T/2 = 3044 \times 3/2^8 = 35.6719$) days for variables in Sect. 4.3. The budget equation for kinetic energy perturbation (EKE) is as follows:

$$\begin{aligned}
\underbrace{\frac{\partial EKE}{\partial t}}_{Tend} &= \frac{\partial}{\partial t}\rho_0 \frac{\left(u^{\sim 1}\right)^2 + \left(v^{\sim 1}\right)^2}{2} \\
&= \underbrace{-\rho^{\sim 1} w^{\sim 1} g}_{BF} \underbrace{- \frac{1}{2}\rho_0 \left\{ \left(\mathrm{v}\mathrm{v}_H\right)^{\sim 1} : \nabla \mathrm{v}_H^{\sim 1} - \left[\nabla \cdot \left(\mathrm{v}\mathrm{v}_H\right)^{\sim 1}\right] \cdot \mathrm{v}_H^{\sim 1} \right\}}_{BT} \\
&\quad \underbrace{- \nabla \cdot \left[\frac{1}{2}\rho_0 \left(\mathrm{v}\mathrm{v}_H\right)^{\sim 1} \cdot \mathrm{v}_H^{\sim 1} + p^{\sim 1}\mathrm{v}^{\sim 1}\right]}_{Q} \\
&\quad \underbrace{+ \mathrm{v}_H^{\sim 1} \cdot \left(A_M \nabla^2 \mathrm{v}_H^{\sim 1} + \frac{\partial}{\partial z}\mu \frac{\partial \mathrm{v}_H^{\sim 1}}{\partial z}\right)}_{D_K}
\end{aligned} \tag{2}$$

Here, $\mathbf{v} = (u,v,w)$ and $\mathbf{v}_H = (u,v)$ represent the full and horizontal velocity vectors, respectively. ρ is the density with reference value ρ_0, and p indicates pressure. A_M denotes the coefficients for horizontal viscosity, and μ is the corresponding vertical mixing coefficients which depend on the local state and mixing parameterization. The operator ∇ represents the three-dimensional gradient operator, and symbol ":" is defined as (**AB**):(**CD**) = (**A**·**B**) (**C**·**D**). The term on the right side of the Eq. (2) describe conversion of energy potential perturbation (EPE) to energy kinetic perturbation through buoyancy forcing (BF, associated with BC), energy transfer from mean flow through BT, nonlocal processes of energy flux divergence Q through advection and pressure work, and energy dissipation D_K through friction, wind stress, and bottom drag. As certain variables are not available in the ECCO2 output, D_K is not explicitly diagnosed and treated as residual in the budget.

A necessary step to estimate the eddy energy budget is to identify the eddy shedding processes. Our method for detecting the eddy shedding consists of two steps. First, the path of the LC jet axis within the GM is determined based on a contour line of a fixed SSH (Sasaki and Minobe 2015). To exclude the influence of seasonal evolution and long-term trend of background flow, the sea level anomaly is used in this study. The anomaly donates as sSLA. $sSLA(x, y, t) = SSH(x, y, t) - \overline{SSH}(t)$, where $\overline{SSH}(t)$ is spatial mean SSH for each time step in the domain region (100°W–75°W, 15°N–35°N). Then, we identify a path of a fixed continuous sSLA contour in the GM in the range from – 2 to 10 cm at 0.5-cm intervals and averaged surface absolute velocity along each continuous contour of 25 years. The results show that absolute velocity reaches maximum along 2.5-cm sSLA isoline, indicative of the main current axis (Fig. 2a). The second step involves calculating length of the LC at each time step and investigating its temporal fluctuation. If the length of the jet decreases by more than 320 km in 3 days (corresponding to diameter of 100 km), we consider this decreasing as an eddy detachment.

4 Results

4.1 The evaluation of ECCO2

Before exploring the eddy generation mechanism in the GM region, it is necessary to quantify whether ECCO2 can capture the characteristics of the LC and its eddy shedding as observed by satellite. Figure 2a and b show the mean and standard deviation of sSLA fields derived from ECCO2 and satellite observation, respectively. The pattern of the ECCO2-simulated LC resembles that from satellite observation. It enters the GM from the Caribbean Sea through the YC and then turns to northeast of the Campeche Bank, forming an intense anticyclonic flow. Finally, the LC enters the Atlantic Ocean through the Florida Strait and joins the Gulf Stream. The transport of the LC at YC is 23.6 Sv, which is also close to previous observations (e.g., Candela et al. 2002, 2019; Sheinbaum et al. 2002). In addition to the mean circulation, sSLA standard deviation reveals that both oceanic variability reaches maximum in the vicinity of the large meander. According to previous study, this

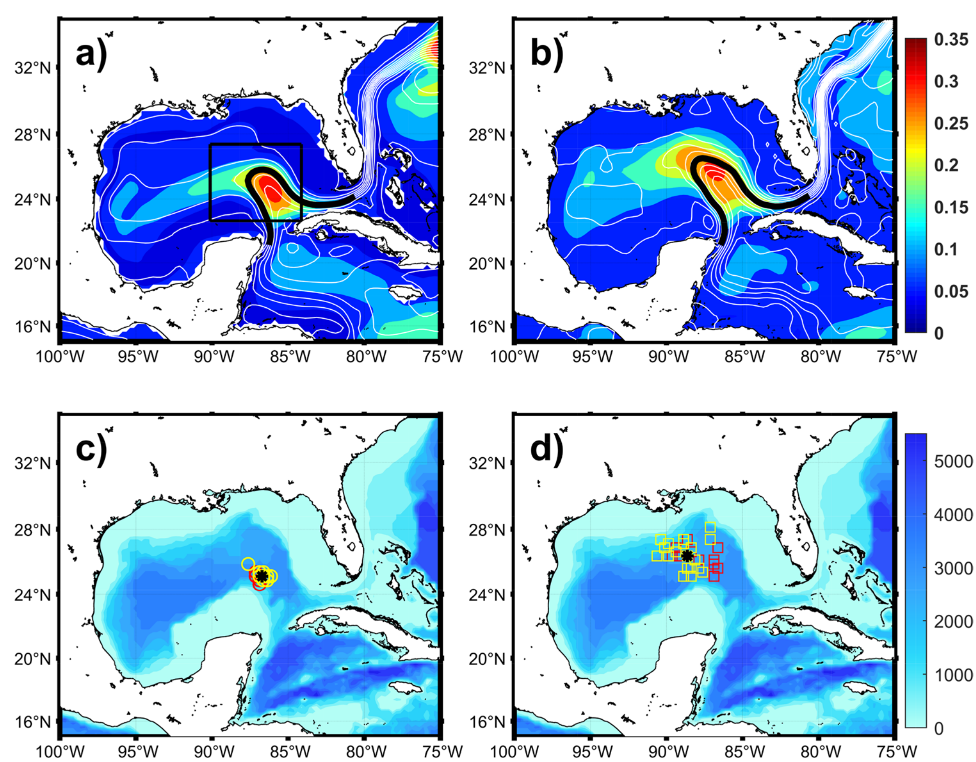

Fig. 2 **a** sSLA (spatial mean SSH within 100°W-75°W,15°N-35°N is excluded) field (contour; unit: cm) and its standard deviation (colored shading; unit: cm) in the Gulf of Mexico from ECCO2. The thick black line denotes the axis of Loop Current. The black box indicates the area for eddy shedding energy budget analysis; **b** the same as (**a**) but based on satellite data. The thick black line denotes the axis of Loop Current. **c** Bathymetry of the GM (shading; m) and eddy centers at the time of detachment (circles). Red and yellow circles indicate category 1 and category 2 (last detachment), respectively. **d** The same as (**c**) but based on satellite data. The black stars in (**c**) and (**d**) are the averaged positions of eddy centers at the time of detachment

maximum reflects the meander and eddy shedding processes (Yang et al. 2020). Moreover, eddies are found to be shed at 87.3°W ± 0.5°, 25.3°N ± 0.3° (eddy center when it is pinched-off, Fig. 2a,c) in ECCO2, which is also close to 88.0°W ± 2.1°, 26.2°N ± 1.9° (Fig. 2b,d) satellite observation. This suggests that ECCO2 reasonably simulates both the mean state and variability in the GM region.

Based on ECCO2, eddy shedding of the LC can be divided into two categories: (1) After an eddy is shed, it migrates southwestward directly and eventually decays in the western GM, and (2) the shed eddy rejoins the LC and detaches from the LC again within the following 3 months, and then it moves southwestward and decays. To make the statistical analysis more confident, here we define the occurrence as an eddy shedding event when the westward-moving eddy crosses the 90°W line. According to this definition, 34 events are identified in 25 years based on the ECCO2, indicative of a frequency about 8.8 month^{-1} on average. This result is close to satellite data (8.5 month^{-1}) and previous studies (Sturges and Leben 2000; Chang and Oey 2011). It should be noted that more shed eddies move westward directly in ECCO2 (21 events in category 1 and 13 events in category 2, Fig. 2c), whereas they tend to rejoin the LC in observation (14 events in category 1 and 20 events in category 2, Fig. 2d). This discrepancy indicates that ECCO2 is not appropriate to investigate the process of eddy reattaching to the LC. For events belonging to category 2, we will focus on the time before the first detachment and after the last detachment.

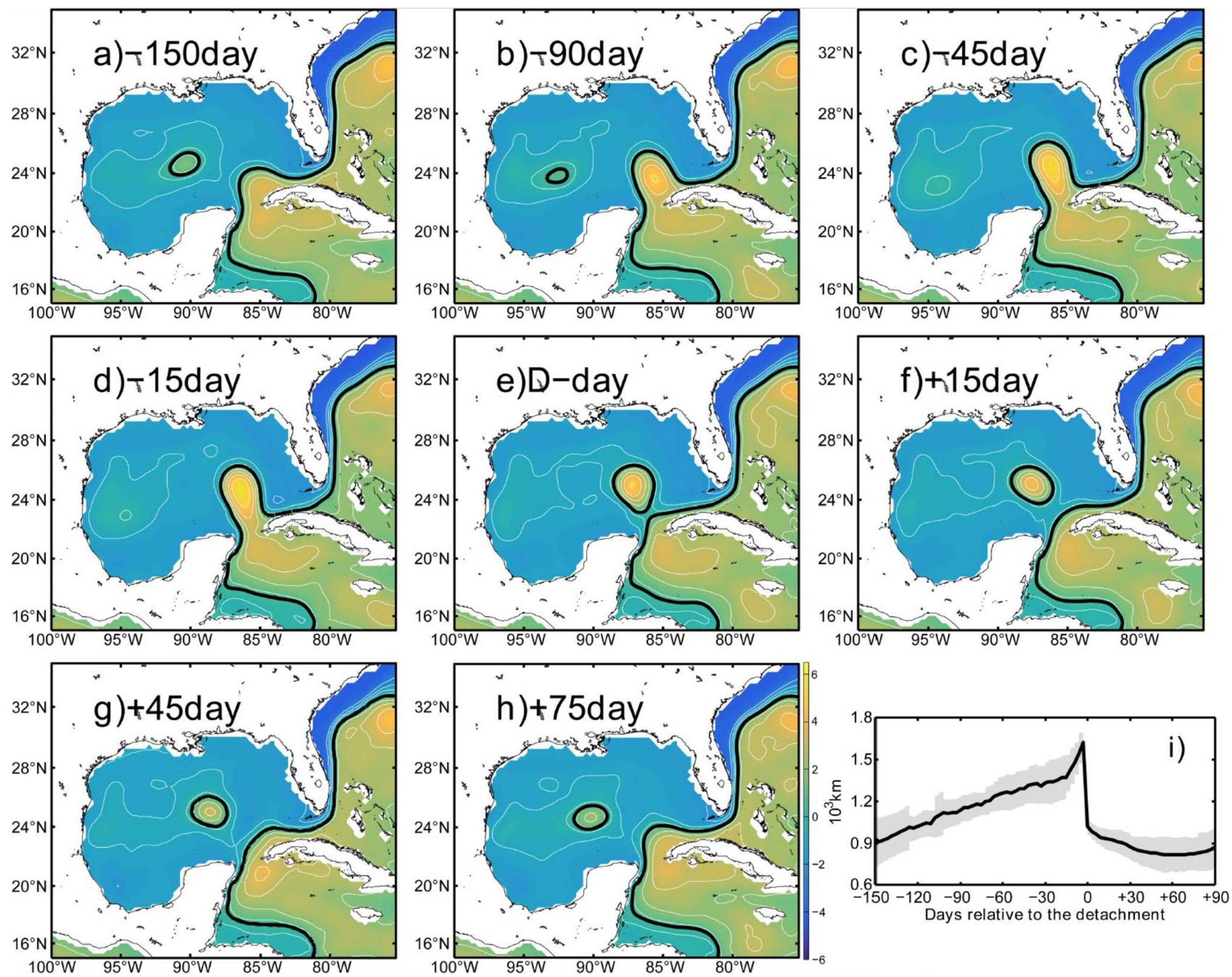

Fig. 3 The ensemble maps for the 34 events with time indicating the days relative to the date of eddy detachment (**a**)–(**h**). Ensemble of sSLA is shaded with color (unit: cm). White contour in the range from – 3 to 6 cm at 1.5-cm intervals. The thick black line in (**a**) ~ (**h**) denotes the ensemble axis of loop current (2.5 cm sSLA isoline). The time of panel in (**a**) ~ (**h**) denotes days before (negative value) or after (positive value) the detachment. **i** The ensemble length of the LC (black thick line) with time indicating the days relative to the date of eddy detachment. The gray shading is the standard deviation of 34 events

4.2 Energetics of the eddy shedding

Figure 3 shows the ensemble sSLA maps for the 34 eddy shedding events with time indicating the days passed since the date of eddy detachment (for events with more than one detachment, time indicates the days before the first detachment and after the last detachment). In 150 ~ 45 days before shedding, the meander of the LC begins to form at the north of the YC and expands northward (Fig. 3a-c). Accompanied by its northward penetration, the LC strengthens, and its length continually elongates (Fig. 3i). In Fig. 3c, a prominent negative sSLA center begins to appear at the southeastern side of the LC (83.4°W, 24.13°N), and then it quickly strengthens in the following period and squeezes the east part of the LC (Fig. 3d). Finally, the neck of the meander is pinched off (Fig. 3e), resulting in the detachment of the anticyclonic eddy (Fig. 3f). The LC sharply shortens at the time of eddy detached from the LC (Fig. 3i). Meanwhile, the LC axis retreats to the south and flows along the north coast of Cuba (Fig. 3g). The westward speed of the pinched-off eddy is about 4.5 cm/s, consistent with observations (Vukovich 2007). Seventy-five days after the detachment, it enters the western Gulf and eventually decays (Fig. 3h,a and b). Accompanied by the above processes, the LC begins to reform (Fig. 3i), and the cycle repeats. One thing should be noted that these 34 cases present high regularity, which is idealized but still an advantage for understanding the processes and underlying dynamics.

To clarify the dominant energy sources and sinks during this process, we examine the energy budget based on Eq. (2). Figure 4 presents the ensemble energy terms based on 34 eddy shedding events integrated in the upper 1500 m layer within selected region (Fig. 2). BT prominently dominates the energy budget in the process of eddy shedding (Fig. 4). Energy transfers from mean flow to eddy. To get a better understanding of the dynamics, spatial distribution of 1500-m-integrated BT (Fig. 5a-c) and BF (Fig. 5d-f) are also provided. In stage1 (– 150 to – 45 days), the LC intrudes and penetrates northward (Fig. 5a). Significant barotropic energy conversion is found along the LC, especially near its western part (Fig. 5a). Meanwhile, the net contribution of BF is negative (Fig. 4), indicating that energy flux from EKE backs to EPE. The LC system moves westward, resulting in the intrusion to Campeche Bank. The returning flow of LC comes across the topography, leading to the upwelling of denser water. During stage 1, the EKE tendency is positive (0.06 W/m^2) but pretty small, and most of the generated energy is balanced by D_K (Fig. 4). After the LC is well developed, its neck is squeezed and finally pinched off (– 45 to + 15 days, stage 2). An anticyclonic eddy is shed from the LC. A remarkable positive EKE tendency (0.3 W/m^2) consists with the development of the eddy. The EKE tendency integrated over the up 1500 m reaches 0.7×10^9 W (Fig. 4). The growth of EKE is inhomogeneous. The EKE reaches the maximum around the day of eddy detachment. Compared to stage 1, BT experiences a significant increase caused by the much stronger shear and strain of the current. In particular, strong released barotropic energy is found at both the western part of the LC and the neck of the meander (Fig. 5b). By contrast, BF presents negative values in the vicinity of the LC, indicating more energy stored as EPE. BF makes minor contribution to the generation of eddy shedding. In stage2, parts of generated energy are diverged through BF and dissipated by D_K (Fig. 4). After the detachment (+ 15 to + 90 days, stage 3), the anticyclonic eddy moves westward, and the energy transfer terms shrink (Figs. 4 and 5c,f). The YC "directly" leaves the GM through the Florida Strait (Fig. 5c). Two things should also be noted. First, the magnitude of BT is four times greater than BF (Fig. 5; note the different scales used for upper and lower panels in Fig. 5), proving that the released barotropic energy is the energy source of eddy shedding process, which is obtained by Yang et al. (2020) as well, and the contribution of BF can be neglected. Second, the nonlocal processes (Q) play the energy sink during the cycle of eddy shedding (Fig. 4). The value of Q cannot be ignored compared to the others in each stage. The details of pressure work's contribution will be discussed in Sect. 5.

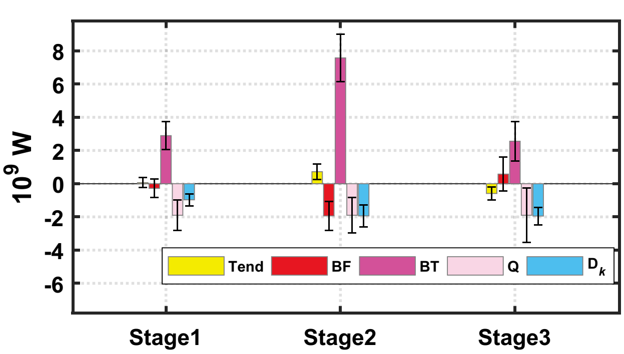

Fig. 4 The ensemble EKE budget integrated over the up 1500 m in the selected region (Fig. 2a). Errors bars indicate the standard deviation of 34 cases

4.3 Energetics of cyclonic eddy

Ensemble analysis of 34 events in the last subsection indicates the existence of the cyclonic eddy at the southeastern side of the LC before eddy shedding (Fig. 3c,d). Besides the ECCO2, the cyclonic eddy is detected in observation as well. Thirty-two of those thirty-four eddy shedding events with observing cyclones are found in the southeastern side of the LC from satellite data. Previous research found cyclonic eddies could be generated around the LC as consequence of

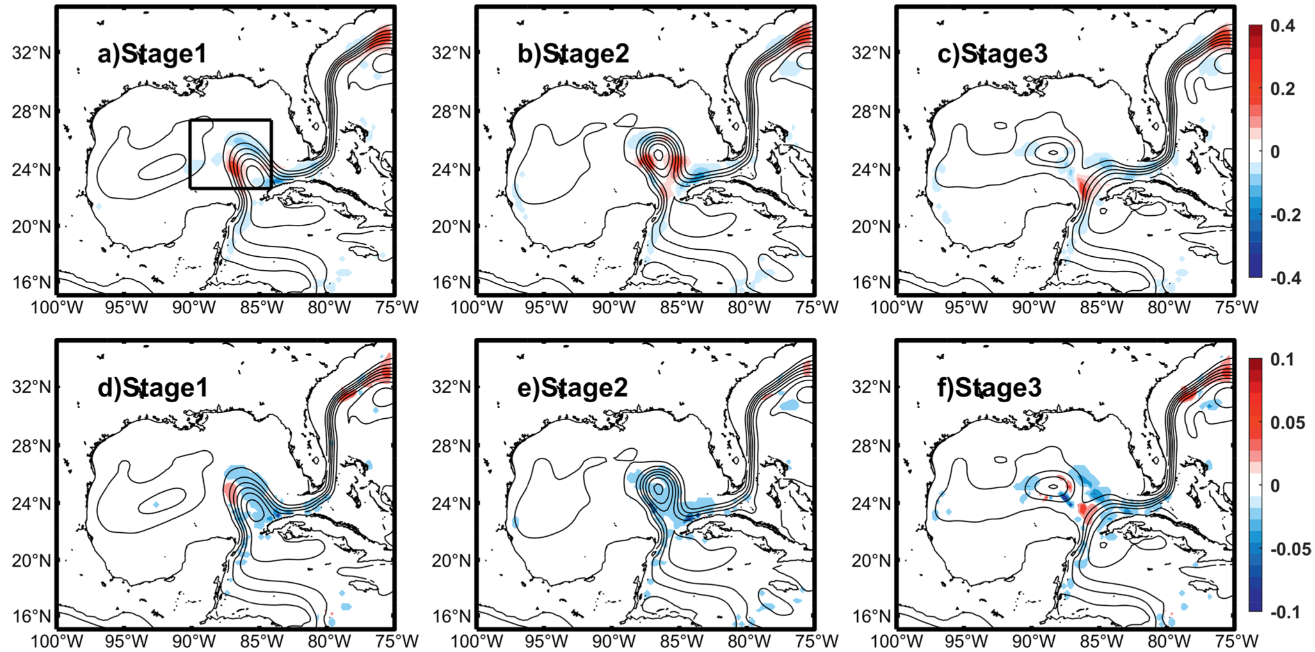

Fig. 5 Ensemble horizontal distribution (colored shading; unit: W/m^2) of BT (**a**) ~ (**c**) and BF (**d**) ~ (**f**). Contours are coinstantaneous mean sSLA isolines. The black box indicates the area for energy budget analysis

BT and BC (e.g., Vukovich et al. 1979; Elliot, 1979; Hurlburt 1986; Chérubin et al. 2006) or by the advection of YC (Candela et al. 2002; Athie et al. 2012). Therefore, we select the region (90°W-84°W, 23°N-27.5°N, black box in Fig. 7a) to investigate the cyclonic eddy. Next, we will explore its generation mechanism through energetic analysis based on Eq. (2). Considering the fast-growing nature of this cyclonic eddy, the cutoff period between mean flow and perturbation is modified to 72 days. Then, the terms of Eq. (2) are calculated for budget analysis.

Through case-by-case investigation, cyclonic eddy can be captured before anticyclonic eddy detachment based on the simulation of ECCO2. To clarify the dominant energy

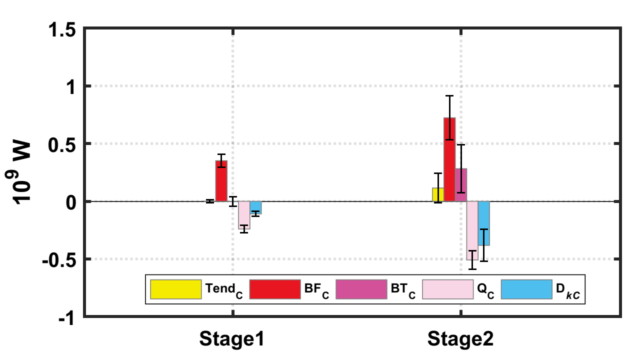

Fig. 6 The ensemble EKE budget integrated over the up 1500 m in the selected region (90°W-84°W, 23°N-27.5°N). Errors bars indicate the standard deviation of 34 cases. Subscript of each term represents cyclonic eddy

source for the cyclonic eddy, Fig. 6 presents the energy budget in stage 1 and stage 2, which are used for the anticyclonic eddy. The significant energy convergences are BF_C and BT_C (Fig. 6, subscript C means the energy flux of cyclonic eddy). The mean flow (period over 72 days) transfers energy to cyclonic eddy. To further understand the contribution of each term, the spatial distribution of main energy source is shown in Fig. 7 (different scales are used for upper and lower panels in Fig. 7). During stage 1, BF_C dominates the energy budget. The denser water from the north sinks in the east part of the LC, indicative of the potential energy release. Remarkable positive values occur in the eastern part of the LC (Fig. 7c). Meanwhile, the alternatively positive and negative values of BT_C along the axis make no effectivity contribution to the generation of cyclonic eddy (Fig. 7a). The generated energy is balanced by the nonlocal divergence term Q_C and energy dissipation term D_{KC}. With the development of the meander, the value of spatially integrated BF_C has doubled compared with that in stage 1 (Fig. 6). EKE gets more energy from EPE due to BC. In this stage, BT_C makes great contribution to the generation of cyclonic eddy, which accounts for 28% of the energy source. Significant barotropic energy conversion is found along the LC, which can reach 0.06 W/m^2, especially near its eastern part (Fig. 7b). The local value of BT_C is twice than that of BF_C (Fig. 7b,d). Similar to the GM scenario, energetics of the cyclonic eddy generated from the Kuroshio Loop in the Luzon Strait are also studied. Zhang et al. (2017) point out that the energy for eddy pairs

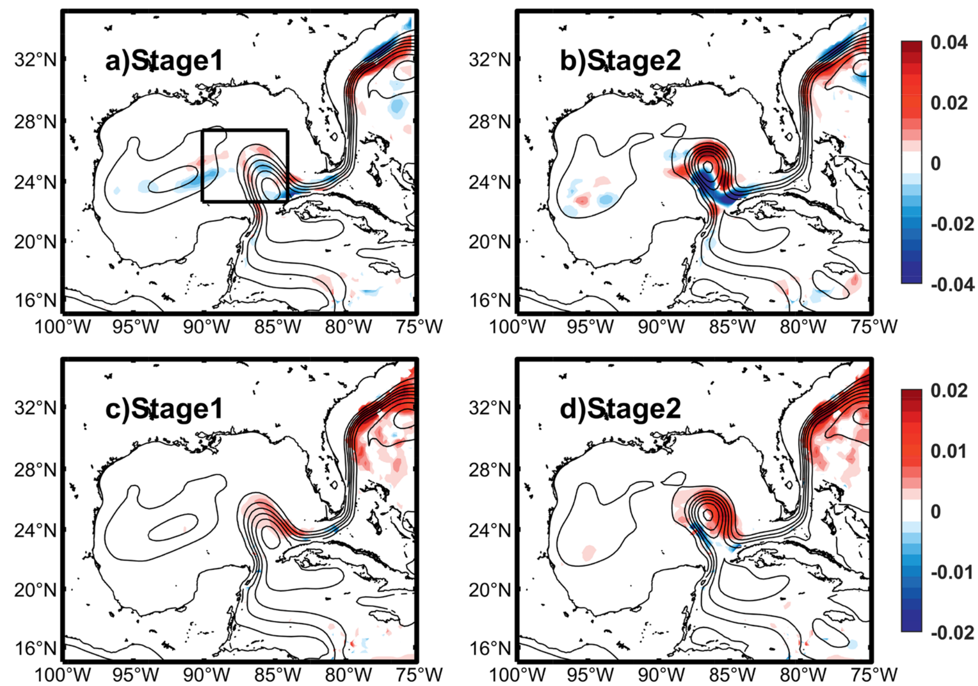

Fig. 7 Ensemble horizontal distribution (colored shading; unit: W/m^2) of BT_C (**a**) ~ (**b**) and BF_C (**c**) ~ (**d**). Contours are coinstantaneous mean sSLA isolines. The black box in (**a**) indicates the area for energy budget analysis

southwest of Taiwan is primarily from BT of the mean flow. The net energy of BT_C integrated in selected region is smaller than that of BF_C resulting in the energy divergence in the eastern part of the LC. The negative value of BT_C suggests energy transfer from EKE back to mean flow. To sum up, BF is the main energy source for the generation of cyclonic eddy based on the composed results; meanwhile, BT also plays an indispensable role.

5 Discussion

Vertical velocity is hard to observe. The BF cannot be diagnosed from observation data. BC is used in energy analysis. Based on the MS-EVA (Liang 2016), $BC = -\frac{g^2}{2\rho_0 N^2}\left\{(v\rho)^{\sim 1}\cdot\nabla\rho^{\sim 1} - \left[\nabla\cdot(v\rho)^{\sim 1}\right]\cdot\nabla\rho^{\sim 1}\right\}$ BC_C (subscript C means the energy flux of cyclonic eddy) is calculated. The mean state of BC_C is combined from stage 1 and stage 2. Ensemble horizontal distribution of (Fig. 8a) shares the similar horizontal distribution with BF_C. The spatial-integrated BC_C and BF_C vary consistently (Fig. 8b). BF_C accounts for 32% of the value of BC_C based on ECCO2. One thing should be noted that ECCO2 cannot find cyclonic eddy in west part of the LC. This is discrepancy with satellite observation, and reasons are unclear.

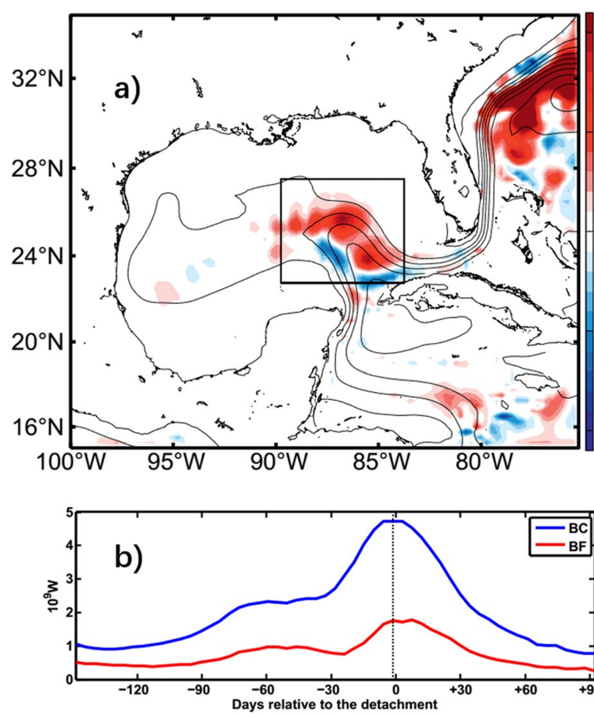

Fig. 8 **a** The mean state of ensemble horizontal distribution (colored shading; unit: W/m.^{2}) of BC. **b** The integrated BC (red) and BF (blue) in black box of (**a**)

During the cycle of eddy shedding process, the nonlocal processes of energy flux divergence Q obviously is negative to the generated energy (Fig. 4). This term includes the process of advection and pressure work. Maslo et al. (2020) find that 75% of the energy maintaining deep kinetic energy is transferred from upper layer to deep layer via PW. Therefore, we pay attention to the effect of PW during the cycle of eddy shedding. The term of Q in Eq. (2) is split into the flux of PW and other nonlocal process of energy flux divergence (Q_K) components:

$$Q = \underbrace{-\nabla \cdot \left[\frac{1}{2}\rho_0 (\mathrm{v}\mathrm{v}_H)^{\sim 1} \cdot \mathrm{v}_H^{\sim 1}\right] - \nabla_H \cdot \left(p^{\sim 1}\mathrm{v}_H^{\sim 1}\right)}_{Q_K} \underbrace{- \frac{\partial}{\partial z}\left(p^{\sim 1}w^{\sim 1}\right)}_{PW} \tag{3}$$

where w is the vertical velocity and. $\nabla_H = \frac{\partial}{\partial x}\vec{i} + \frac{\partial}{\partial y}\vec{j}$ Taking Eq. (3) into Eq. (2), the budget equation can be written as follows:

$$\underbrace{\frac{\partial EKE}{\partial t}}_{Tend} = \underbrace{-\rho^{\sim 1}w^{\sim 1}g}_{BF} \underbrace{-\frac{1}{2}\rho_0\left\{(\mathrm{v}\mathrm{v}_H)^{\sim 1} : \nabla \mathrm{v}_H^{\sim 1} - \left[\nabla \cdot (\mathrm{v}\mathrm{v}_H)^{\sim 1}\right] \cdot \mathrm{v}_H^{\sim 1}\right\}}_{BT}$$
$$\underbrace{-\nabla \cdot \left[\frac{1}{2}\rho_0 (\mathrm{v}\mathrm{v}_H)^{\sim 1} \cdot \mathrm{v}_H^{\sim 1}\right] - \nabla_H \cdot \left(p^{\sim 1}\mathrm{v}_H^{\sim 1}\right)}_{Q_K}$$
$$\underbrace{-\frac{\partial}{\partial z}\left(p^{\sim 1}w^{\sim 1}\right)}_{PW} \underbrace{+\mathrm{v}_H^{\sim 1} \cdot \left(A_M \nabla^2 \mathrm{v}_H^{\sim 1} + \frac{\partial}{\partial c}\mu \frac{\partial \mathrm{v}_H^{\sim 1}}{\partial z}\right)}_{D_K} \tag{4}$$

To clarify the effect of PW during eddy shedding process, we examine the energy budget based on Eq. (4). The cutoff between eddy and mean flow is designed as 285 days. Figure 8a presents the budget below 1500 m in the whole region of GM, which is obviously dominated by PW. This indicates that PW is the main energy source of abyssal ocean in selected frequency. Positive value means that energy flux transfers from upper layer to the deep layer. Other nonlocal process of energy flux divergence can be ignored during eddy shedding (Fig. 9a). Below 1500 m, energy is transferred though PW and dissipated by D_K. Before the eddy detachment from LC, the abyssal ocean is inactive. When eddy shed from LC, the energy transfers to the abyssal ocean through PW (Fig. 9b). The value of integrated EKE below 1500 m sharply increases at eddy shed. With the eddy moving westward in the upper ocean, the energy flux of PW and spatial-integrated EKE consistently decrease. Lagrange tracking is employed to investigate the work of PW on eddy in the upper 1500 m. A box (2.5°×2.5°) tracks the eddy after detachment. The center of box is the position of eddy center. After eddy shed, EKE decreases with detachment day from LC. Only less than 40% of the EKE has been left in 120 days since detachment day. Tracking the eddy, the integrated PW can reach nearly 3×10^8 J in the coinstantaneous time. Approximately 50% of the dissipation of EKE is transferred from the upper layer to the deep layer by PW.

6 Conclusions

Based on the ECCO2 data from 1992 to 2016 through the MS-EVA, the energetics during eddy shedding process in the GM are explored in this study. ECCO2 can capture the main characteristics of GM. The climatological Yucatan Transport is 23.6 Sv derived from ECCO2. During 1992 to 2016, 34 eddy shedding events are captured by ECCO2, out of which 21 eddies are moving directly westward after shedding from LC, and 13 eddies rejoin the LC and detach again. The ensemble analysis reveals that BT is the main energy source of eddy shedding; meanwhile, the BF is not contributing to the energy source during eddy shedding period. During the stage of eddy shedding, energy transfers from upper layer to the deep layer

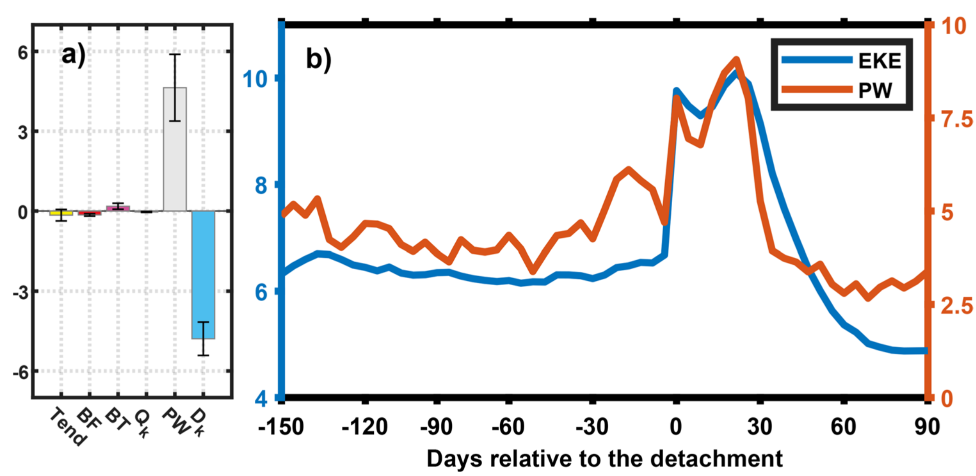

Fig. 9 **a** The ensemble mean stage of EKE budget integrated over the below 1500 m in the Gulf of Mexico (unit: 10^8 W). Errors bars indicate the standard deviation of 34 cases. **b** The ensemble energy flux of PW (red, unit: 10^8 W) and EKE (blue, unit: 10^{14} J) with time indicating the days relative to the date of eddy detachment

by PW. The PW is the main source of abyssal EKE, in accordance with the previous study (Maslo et al. 2020).

ECCO2 can also capture the cyclonic eddy before eddy shedding in the eastern side of the LC. In previous research (e.g., Oey 2008; Xu et al. 2013), BC is what generates the process. Based on ECCO2 results, the integrated BF dominates the energy budget. However, BT also plays significant role on generation of cyclonic eddy. The value of BT is as twice as that of BF in the region of eastern part of the LC. In previous research based on site observations, BC, instead of BF, is usually diagnosed because of the lack of vertical velocity. Even though BC changes in pace with BF, the latter only accounts for 30% of the value of BC. This leads to the underestimating of barotropic instability's effect on generation of cyclonic eddy. Based on the results, BT is comparable to BC for the contribution of eddy generation.

Several problems remain. In ECCO2 simulation, the period of eddy shedding case is more uniform than observations. Meanwhile, in observation, the process of eddy shedding is more complex, and more eddy shedding events belong to category 2. Answers may be found by improving the spatial and temporal resolution of model. The simulation of cyclonic eddy is not perfect; the generation of cyclonic eddy needs further study. Other energetics methods (e.g., Chen et al. 2014; Kang and Curchitser 2015) should be analyzed. As a part of AMOC, the transport of the LC may vary in low frequency, which may modulate the eddy shedding process. Therefore, the variation of eddy shedding in low frequency is expected to be investigated in future studies using high-resolution couple models.

Acknowledgements This work has been carried out at Physical Oceanography Laboratory/Ocean University of China, China. The authors would like to thank laboratory for providing all needed support to carry out this research. Comments and suggestions from two anonymous reviewers and the editor greatly helped improve the manuscript. All the analysis and plotting are done in MATLAB.

Funding This research is supported by National Natural Science Foundation of China (42176006, 42106014), Fundamental Research Funds for the Central Universities (202072001, 202241006), Postdoctoral Innovation Project of Shandong Province (202003012), and Taishan Scholar Funds (tsqn201812022).

Data availability The datasets generated and/or analyzed in the current study are available from the corresponding author on reasonable request. The following dataset are used for the analysis: ECCO2 dataset is downloaded from http://apdrc.soest.hawaii.edu/data/; Satellite data sourced from https://resources.marine.copernicus.eu/product-detail/.

Code availability Codes for the energy budget can be available from corresponding author.

Declarations

Conflict of interest The authors declare no competing interests.

References

Adcroft A, Campin JM, Hill C, Marshall J (2004) Implementation of an atmosphere–ocean general circulation model on the expanded spherical cube. Mon Weather Rev 132:2845–2863

Androulidakis Y, Kourafalou V, Le Henaff M (2014) Influence of frontal cyclone evolution on the 2009 (Ekman) and 2010 (Franklin) Loop Current eddy detachment events. Ocean Sci 10:947–965

Athie G, Candela J, Ochoa-de-la-Torre J, Sheinbaum J (2012) Impact of Caribbean cyclones on the detachment of Loop Current anticyclones. J Geophys Res 117:C03018

Athie G, Sheinbaum J, Candela J et al (2020) Seasonal variability of the transport through the Yucatan Channel from observations. J Phys Oceanogr 50(2):343–360

Buckley M, Marshall J (2016) Observations, inferences, and mechanisms of the Atlantic Meridional Overturning Circulation: a review. Rev Geophys 54:5–63

Bunge L, Ochoa-de-la-Torre J, Badan A et al (2002) Deep flows in the Yucatan Channel and their relation to changes in the Loop Current extension. J Geophys Res 107(C12):3233

Candela J, Ochoa J, Sheinbaum J et al (2019) The flow through the Gulf of Mexico. J Phys Oceanogr 49:1381–1401

Candela J, Sheinbaum J, Ochoa-de-la-Torre J et al (2002) The potential vorticity flux through the Yucatan Channel and the Loop Current in the Gulf of Mexico. Geophys Res Lett 29:2059

Chang YL, Oey LY (2011) Loop current cycle: coupled response of the Loop Current with deep flows. J Phys Oceanogr 41:458–471

Chang YL, Oey LY (2012) Why does the Loop Current tend to shed more eddies in summer and winter? Geophys Res Lett 39(5):L05605

Chang YL, Oey LY (2013) Loop Current growth and eddy shedding using models and observations: numerical process experiments and satellite altimetry data. J Phys Oceanogr 43:669–689

Chen R, Flierl G, Wunsch C (2014) A description of local and nonlocal eddy-mean flow interaction from an eddying state estimate. J Phys Oceanogr 44(9):2336–2352

Chérubin LM (2005) Deep flow variability in the vicinity of the Yucatan Straits from a high-resolution numerical simulation. J Geophys Res 110(C4):C04009. https://doi.org/10.1029/2004JC002280

Chérubin LM, Morel Y, Chassignet EP (2006) Loop current ring shedding: the formation of cyclones and the effect of Topography. Journal of Physical Oceanography 36(4):569–591. https://doi.org/10.1175/JPO2871.1

Chiri H, Abascal AJ, Castanedo S, Antolínez JAA, Liu Y, Weisberg RH, Medina R (2019) Statistical simulation of ocean current

patterns using autoregressive logistic regression models: a case study in the Gulf of Mexico. Ocean Modelling 136:1–12
Cochrane JD (1972) Separation of an anticyclone and subsequent developments in the Loop Current (1969). In Contributions on the Physical Oceanography of the Gulf of Mexico, 1st edn. Gulf Pub, Houston, pp 91–106
Cooper C, Forristall G, Joyce T (1990) Velocity and hydrographic structure of two Gulf of Mexico warm-core rings. J Geophys Res 95:1663–1679
Donohue KA, Watts D, Hamilton PE et al (2016) Loop Current eddy formation and baroclinic instability. Dyn Atmos Oceans 76:195–216
Ducet N, Traon P-Y, Reverfdin G (2000) Global high-resolution mapping of ocean circulation from TOPEX/Poseidon and ERS-1 and -2. J Geophys Res 105:19477–19498
Enfield D, Mestas-Nunez A, Trimble P (2001) The Atlantic Multidecadal Oscillation and its relation to rainfall and river flows in the continental U.S. Geophys Res Lett 28:2077–2080
Forristall G, Schaudt K, Cooper C (1992) Evolution and kinematics of a Loop Current eddy in the Gulf of Mexico during 1985. J Geophys Res 97:2173–2184
Fratantoni P, Lee T, Podesta G, Muller-Karger F (1998) The influence of Loop Current perturbations on the formation and evolution of Tortugas Eddies in the southern straits of Florida. J Geophys Res 103:24759–24779
Hamilton P (1992) Lower continental slope cyclonic eddies in the central Gulf of Mexico. J Geophys Res 97(C2):2185–2200
Hamilton PE (2019) The Loop Current: observations of deep eddies and topographic Rossby waves. J Phys Oceanogr 49(6)
Hong X, Chang S, Raman S et al (2000) The Interaction between Hurricane Opal (1995) and a Warm Core Ring in the Gulf of Mexico. Mon Weather Rev 128:1347–1365
Huang H (2013) An analysis of Loop Current frontal eddies in a 1/ 6 Atlantic Ocean model simulation. J Phys Oceanogr 43:1924–1939
Hurlburt H (1986) Dynamic transfer of simulated altimeter data into subsurface information by a numerical ocean model. J Geophys Res 91:2372–2400
Hurlburt HE, Thompson JD (1980) A numerical study of Loop Current intrusions and eddy shedding. J Phys Oceanogr 10:1611–1651
Kang D, Curchitser EN (2015) Energetics of eddy–mean flow interactions in the gulf stream region. J Phys Oceanogr 45:1103–1120
Large W, McWilliams J, Doney S (1994) Oceanic vertical mixing: a review and a model with a nonlocal boundary layer parameterization. Rev Geophys 32:363–403
Le Hénaff M, Kourafalou V, Morel Y, Srinivasan A (2012) Simulating the dynamics and intensification of cyclonic Loop Current Frontal Eddies in the Gulf of Mexico. J Geophys Res 117:C02034
Liang XS (2016) Canonical Transfer and multiscale energetics for primitive and quasigeostrophic atmospheres. J Atmos Sci 73:4439–4468
Liu Y, Weisberg RH, Vignudelli S, Mitchum GT (2016) Patterns of the loop current system and regions of sea surface height variability in the eastern Gulf of Mexico revealed by the self-organizing maps. J Geophys Res Oceans 121(4):2347–2366. https://doi.org/10.1002/2015JC011493
Lugo-Fernández A, Leben RR, Hall CA (2016) Kinematic metrics of the Loop Current in the Gulf of Mexico from satellite altimetry. Dyn Atmospheres Oceans 76:268–282
Marshall J, Adcroft A, Hill C et al (1997) A finite-volume, incompressible Navier Stokes model for studies of the ocean on parallel computers. J Geophys Res 102:5753–5766
Maslo A, de Souza JMAC, Pardo JS (2020) Energetics of the Deep Gulf of Mexico. J Phys Oceanogr 50:1655–1675
Menemenlis D, Hill C, Adcroft A et al (2005) NASA supercomputer improves prospects for ocean climate research. EOS Trans Am Geophys Union 86:89–96
Murphy S, Hurlburt H, O'Brien J (1999) The connectivity of eddy variability in the Caribbean Sea, the Gulf of Mexico, and the Atlantic Ocean. J Geophys Res 104:1431–1453
Nof D (2005) The momentum imbalance paradox revisited. J Phys Oceanogr 35:1928–1939
Oey L-Y, Lee H-C (2002) Deep eddy energy and topographic Rossby waves in the Gulf of Mexico. J Phys Oceanogr 32:3499–3527
Oey L-Y (1996) Simulation of mesoscale variability in the Gulf of Mexico. J Phys Oceanogr 26:145–175
Oey L-Y (2004) Vorticity flux through the Yucatan Channel and Loop Current variability in the Gulf of Mexico. J Geophys Res 109:C10004
Oey L-Y (2008) Loop Current and Deep Eddies. J Phys Oceanogr 38:1426–1449
Oey L-Y, Ezer T, Lee H-C (2005) Loop Current, rings and related circulation in the Gulf of Mexico: a review of numerical models and future challenges. Geophys Monograph Ser 161:31–56
Paluszkiewicz T, Atkinson L, Posmentier E, Mcclain C (1983) Observations of a loop current frontal eddy intrusion onto the West Florida Shelf. J Geophys Res 88:9639–9651
Pichevin T, Nof D (1997) The Momentum Imbalance Paradox Tellus A 49:298–319
Rudnick D, Gopalakrishnan G, Cornuelle B (2015) Cyclonic eddies in the Gulf of Mexico: observations by underwater gliders and simulations by numerical model. J Phys Oceanogr 45:313–326
Sasaki Y, Minobe S (2015) Climatological mean features and interannual to decadal variability of ring formations in the Kuroshio Extension region. J Oceanogr 71(5):499–509
Shay LK (2009) Upper ocean structure: responses to strong atmospheric forcing events. Encyclopedia of Ocean Sciences, 2nd edn. Elsevier, Amsterdam, pp 192–210
Sheinbaum J, Candela J, Badan A, Ochoa-de-la-Torre J (2002) Flow structure and transport in the Yucatan Channel. Geophys Res Lett 29:1040
Sturges W (1994) The frequency of ring separations from the Loop Current. J Phys Oceanogr 24(7):1647–1651
Sturges W, Leben R (2000) Frequency of ring separations from the Loop Current in the Gulf of Mexico: a revised estimate. J Phys Oceanogr 30:1814–1819
Vukovich F, Crissman B, Bushnell M, King W (1979) Some aspects of the oceanography of the Gulf of Mexico using satellite and in situ data. J Geophys Res 84:7749–7768
Vukovich FM, Maul GA (1985) Cyclonic eddies in the Eastern Gulf of Mexico. J Phys Oceanogr 15:105–117
Vukovich FM (1988) Loop Current boundary variations. J Geophys Res 93(C12):15585–15591
Vukovich FM (2007) Climatology of ocean features in the Gulf of Mexico using satellite remote sensing data. J Phys Oceanogr 37:689–707
Weisberg RH, Liu Y (2017) On the loop current penetration into the Gulf of Mexico. J Geophys Res Oceans 122(12):9679–9694. https://doi.org/10.1002/2017JC013330
Welsh SE, Inoue M (2000) Loop Current rings and the deep circulation in the Gulf of Mexico. J Geophys Res: Oceans 105:16951–16959
Wunsch C, Heimbach P, Ponte RM, Fukumori I, and the ECCO-GODAE Consortium Members (2009) The global general circulation of the ocean estimated by the ECCO-Consortium. Oceanography 22(2):88–103
Xu F, Chang Y-L, Oey L-Y, Hamilton PE (2013) Loop Current growth and eddy shedding using models and observations: analyses of the July 2011 eddy-shedding event. J Phys Oceanogr 43:1015–1027
Yang H, Qiu B, Chang P et al (2018) Decadal variability of eddy characteristics and energetics in the Kuroshio extension: unstable versus stable states. J Geophys Res: Oceans 123(8):6653–6669

Yang Y, Weisberg R, Liu Y, Liang XS (2020) Instabilities and multi-scale interactions underlying the Loop Current eddy shedding in the Gulf of Mexico. J Phys Oceanogr 50:1289–1317
Yin X-Q, Oey L-Y (2007) Bred-ensemble ocean forecast of loop current and rings. Ocean Modell 17:300–326
Zavala-Hidalgo J, Morey SL, O'Brien JJ (2003) Cyclonic eddies northeast of the Campeche Bank from altimetry data. J Phys Oceanogr 33:623–629
Zhang Z, Zhao W, Qiu B, Tian J (2017) Anticyclonic eddy sheddings from Kuroshio Loop and the accompanying cyclonic eddy in the Northeastern South China Sea. J Phys Oceanogr 47:1243–1259